



## Experimental analysis of flow pattern and heat transfer in circular-orifice baffled tubes

J. Muñoz-Cámara<sup>a,\*</sup>, D. Crespí-Llorens<sup>b</sup>, J.P. Solano<sup>a</sup>, P.G. Vicente<sup>b</sup>

<sup>a</sup> Dep. Ingeniería Térmica y de Fluidos, Universidad Politécnica de Cartagena, Campus Muralla del Mar, 30202 Cartagena, Spain

<sup>b</sup> Universidad Miguel Hernández, Departamento de Ingeniería Mecánica y Energía, Avda. de la Universidad s/n, 03202 Elche, Spain

### ARTICLE INFO

#### Article history:

Received 30 April 2019

Received in revised form 15 October 2019

Accepted 15 October 2019

Available online 8 November 2019

#### Keywords:

Heat transfer enhancement

Turbulence promoters

Transitional flow

Circular-ring turbulator

Baffled tube

### ABSTRACT

An experimental study on the thermal-hydraulic and flow pattern characteristics of tubes with circular-orifice baffled inserts is performed. A geometry with an orifice-to-tube diameter ratio of  $d/D = 0.5$  and an interbaffle spacing equal to  $1.5D$  is tested in steady-state conditions. Isothermal friction factor tests in the range  $10 < Re < 2200$  allow the laminar, transitional and turbulent flow regimes to be identified. Flow visualization by means of hydrogen bubbles is used to assess the main flow structures and their relation with the onset of transition, which occurs at  $Re \approx 160$ . Heat transfer experiments under uniform heat flux are conducted in order to obtain the Nusselt number as a function of Reynolds number, for  $150 < Pr < 630$ , using propylene-glycol as the test fluid. Numerical simulations are used to complement the visualization study and explain the role of the flow structures on the thermal-hydraulic behavior.

© 2019 Elsevier Ltd. All rights reserved.

### 1. Introduction

Insert devices are widely used means of heat transfer enhancement, which can be installed in smooth tubes of heat exchangers while maintaining their original mechanical strength. Likewise, retrofitting of existing equipment with tube inserts is also a remarkable advantage of this type of devices. Twisted tapes [1–3], wire coils [4,5] and wire meshes [6] are typical designs used as insert devices in heat exchangers. Their geometrical characteristics must be chosen according to the operational conditions of the internal flow, in order to maximize convective heat transfer enhancement, keep pressure drop under reasonable levels and -if applicable- achieve turbulent promotion at low Reynolds number. Equally-spaced circular rings are another typology of insert device, where convective heat transfer is augmented on the basis of the periodic contraction and expansion of the bulk flow. They consist of flat disks with a central orifice, whose open area fraction is typically characterized by the orifice-to-tube diameter ratio  $d/D$ .

A limited number of experimental studies have analyzed the thermal-hydraulic performance of circular rings. Kongkai-paiboon et al. [7] studied the heat transfer and pressure drop characteristics for circular-ring turbulators, testing several diameter ratios ( $d/D = 0.5, 0.6$  and  $0.7$ ) and three pitch ratios,  $L/D$  (free space between baffles divided by the tube inner diameter), achieving a

maximum thermal performance of 7% for the lowest pitch ratio ( $L/D = 6$ ) and the highest  $d/D$  value. Promvong et al. [8] tested inclined annular baffles, varying the relation between the disk thickness and the tube diameter, and the pitch ratio (0.5, 1.0, 1.5, 2.0) for an angle of  $30^\circ$ . A maximum value of 40% was found for the thermal performance for the lowest thickness/diameter ratio and the lowest pitch ratio. Acir et al. [9] studied heat transfer in tubes with annular disks, focusing on the effect of the pitch ratio,  $L/D$ , and the number of orifices over the annulus; a maximum thermal performance of 83% was found for the geometry with two orifices and  $L/D = 2$ . Ruengpayungsak et al. [10] modified the annular geometry to include some semi-circular orifices to achieve a gear-ring geometry; a maximum thermal performance for  $L/D = 3$  of 24%, 26%, 28% and 30% was found for baffles with tooth numbers of 0, 8, 16 and 24. In addition, circular-rings have been used in combination with other geometries as twisted tapes. Eiamsa-ard et al. [11] studied the thermal performance of a tube with twisted-tape and circular ring inserts. Several twist ratios (3.0, 4.0 and 5.0) and pitch ratios (1.0, 1.5 and 2.0) were tested. The maximum thermal performance, 42%, was achieved at the lowest twist and pitch ratios and Reynolds number tested ( $Re \approx 6000$ ). Abolarin et al. [12] tested u-cut twisted tapes with ring inserts, for ring space ratios (the ring insert pitch divided by the tape width) of 1.25, 1.5 and 5.0. The authors obtained earlier transitions and an increase in the pressure drop and the heat transfer when the rings were inserted and the ring space ratio was lower.

\* Corresponding author.

E-mail address: [jose.munoz@upct.es](mailto:jose.munoz@upct.es) (J. Muñoz-Cámara).

## Nomenclature

$c_p$	specific heat ( $\text{J kg}^{-1} \text{K}^{-1}$ )
$C_0$	orifice coefficient (-)
$d$	orifice diameter (m)
$D$	tube inner diameter (m)
$k$	thermal conductivity ( $\text{W m}^{-1} \text{K}^{-1}$ )
$l$	Tube length (m)
$l_{rec}$	recirculation length (m)
$L$	spacing between consecutive baffles, equal to cell length (m)
$L_h$	heated length (m)
$L_p$	distance between pressure ports (m)
$\dot{m}$	mass flow rate (kg/s)
$N$	number of tubes (-)
$q$	net heat transfer rate (W)
$q''$	net heat flux ( $\text{W/m}^2$ )
$R3$	performance evaluation criterion (-)
$S$	open area, $(d/D)^2$ (-)
$t$	Baffle thickness (m)
$T$	Temperature ( $^{\circ}\text{C}$ )
$u$	mean velocity, based on the tube diameter, $D$ (m)
$\dot{W}$	power consumption (W)
$x$	axial distance from the start of the heated area (m)
$\Delta p$	pressure drop (Pa)

## Dimensionless groups

$f$	Fanning friction factor, $\frac{\Delta p}{2\rho u^2} \frac{D}{l}$
$Gr^*$	Modified Grashof number, $g\beta q'' D^4 / kv$
$Nu$	Nusselt number, $hD/k$
$Pr$	Prandtl number, $\mu c_p / k$
$Re$	Reynolds number, $\rho v D / \mu$

## Greek symbols

$\beta$	coefficient of thermal expansion ( $\text{K}^{-1}$ )
$\mu$	dynamic viscosity ( $\text{kg m}^{-1} \text{s}^{-1}$ )
$\nu$	kinematic viscosity ( $\text{Pa s}$ )
$\rho$	fluid density ( $\text{kg m}^{-3}$ )
$\sigma$	standard deviation

## Subscripts

$b$	bulk
$in$	inlet
$j$	section number
$s$	smooth tube
$wi$	inner wall

From these studies, it can be concluded that these inserts show a high thermal performance when their geometry is well selected. It is also remarkable that the majority of them detected the highest thermal performance at the lowest Reynolds number of their tests, which were in almost all cases above  $Re = 3000$ . However, many industrial applications that may require the use of insert devices for heat transfer enhancement purposes work in laminar or transitional flow regimes and high Prandtl number fluids. Furthermore, the effect of Prandtl number on heat transfer in tubes with circular rings is not reported in the open literature, as most experiments only use air as test fluid. Among the cited works, there are remarkable exceptions as the study of Abolarin et al. [12], where water is used as the working fluid and the laminar and transitional flow regimes are studied as well.

In addition to the interest of circular rings as a passive technique, these inserts have spread their applications during the last decades, due to the potential benefit in enhancing mass and heat transfer when an oscillatory flow is superimposed to a net flow. Currently, this configuration is found in oscillatory-baffled reactors (OBR), where the inserts promote the continuous flow separation and reattachment. In OBRs, a high-residence time product flows across the circular tube, yielding very low net flow Reynolds numbers. A piston or bellow connected to the tube provides a superimposed oscillatory flow, which increases the radial mixing and promotes heat and mass transfer intensively [13]. A few number of experimental investigations have shed light on the heat transfer characteristics of OBRs with circular orifice baffles [14–16]. However, the performance of the tube insert in the absence of oscillatory flow is still insufficiently described, correlations for Nusselt number are available only for the turbulent region (Reynolds numbers above 200) and the role of the Prandtl number has not been studied properly. In addition, González-Juárez et al. [17] studied numerically the heat transfer in baffled tubes and reported unrealistic behaviors for the proposed correlations [14,15] after extrapolating at lower Reynolds numbers, because these provided lower heat transfer rates than a smooth tube. The need to increase the studied range of Reynolds numbers is justified by some potential

applications, where the required residence time could be higher, or the fluid has a very high viscosity.

The experimental analysis of the flow pattern in circular rings has also attracted little attention up to date. Kiml et al. [18] performed heat transfer and visualization tests in tubes with transverse and inclined circular rings, with  $d/D = 0.8$ , working in the Reynolds number range of 5000–20,000. Focusing on the transverse ribs, they identified the separation bubbles just behind the ribs and the reattachment point between consecutive ribs. This flow pattern showed a clear influence on the local Nusselt number results; after the flow separation downstream the rib, a sharp drop in heat transfer was noticed past the reattachment point due to the boundary layer growth. Muñoz et al. [19] used the Particle Image Velocimetry technique to study the behavior of the flow in equally-spaced baffles in round tubes with  $d/D = 0.5$ ,  $L/D = 1.5$  and  $20 < Re < 300$ . The measurement of the turbulent intensity and the energy of the fluctuating components of the flow field allowed to assess the unstable nature of the flow for  $Re > 160$ .

Experimental correlations for Fanning friction factor in the low Reynolds number range (e.g.  $Re < 3000$ ) have not been reported so far in the open literature. An attempt to quantify the steady-state pressure drop in net and oscillatory superimposed flows was accounted for in the quasi-steady model proposed by Jealous and Johnson [20]. This model assumes that the pressure drop caused by a steady-state flow along a tube with equally-spaced annular baffles is the same as a series of individual orifices in a turbulent flow, using the discharge coefficient concept. This approach presents two main drawbacks: a) the discharge coefficient is strongly influenced by the flow regime [21], particularly in the laminar and transitional ranges, which advises against the use of a constant discharge coefficient in some applications; b) the interaction of the flow between consecutive baffles is not accounted for if the discharge coefficient is used for evaluating the overall pressure drop.

The present study aims at clarifying some open questions on the thermal-hydraulic characteristics and flow mechanisms in tubes with equally-spaced annular baffles working in the laminar and

transitional flow regimes. A baffle geometry with  $d/D = 0.5$  and pitch ratio of  $L/D = 1.5$  is used as test specimen, following the widely accepted designs for the construction of oscillatory baffled reactors proposed by Ni et al. [22]. Heat transfer tests under uniform heat flux conditions are conducted for a range of net-flow Reynolds number of  $10 < Re < 3000$ , using propylene-glycol as the working fluid at different temperatures, which allows to extend the Prandtl number analysis to the range of  $150 < Pr < 630$ . Friction factor measurements obtained under isothermal conditions are presented in the range  $10 < Re < 3000$ , allowing the transition from laminar to turbulent flow to be identified. The physics of transition are described experimentally using hydrogen bubble visualization, and CFD results are also employed to support the discussion of the impact of the flow structures on the thermohydraulic behaviour.

**2. Experimental test rig**

*2.1. Geometry*

The geometry under study is shown at Fig. 1. The insert baffles are a geometrical annuli fitted to the inner tube wall, with an orifice diameter  $d = 0.5D$ . The baffle spacing is  $1.5D$ . The baffles are made of PEEK plastic (to avoid electrical conduction from the tube wall) with thickness  $t = 1$  mm. They are assembled using three axial rods (1.6 mm diameter).

*2.2. Visualization facility*

The facility depicted in Fig. 2 was built in order to study the flow within the described geometry by using hydrogen bubble visualization.

The test section consists of a  $D = 32$  mm diameter acrylic tube (also depicted in Fig. 2) equally spaced insert baffles which are fixed by three steel rods. The use of the rods has been avoided in the visualization section for better results. Five baffles are placed upstream of the test section and also downstream of it in order to ensure spatial periodicity of the flow field. A flat-sided acrylic box, filled with the same working fluid used in the facility, is placed around the test section for a better optical access.

Heating and final temperature control is carried out by an electric heater located in the upper reservoir tank. A Coriolis flowmeter and a control valve are used to control and monitor the working flow rate.

The visualization by hydrogen bubbles is a qualitative technique that allows the perception of the main flow structures [23]. For that, the hydrogen bubbles are generated by means of a copper wire (cathode) that crosses the tube diametrically upstream of the visualization area, being the anode a metallic component of the circuit located downstream of the test section. Thus, a symmetry plane of the flow is seeded with hydrogen bubbles, while illu-

mination is provided by two rear lamps. A CMOS  $1280 \times 1024$   $\text{pix}^2$  CMOS camera is situated in orthogonal position in relation to that plane, so that it can have a front view of it, or in parallel to it in order to have a side view. The bubbles size and quantity are set up by adjusting the constant voltage, generated by a DC power supply, applied between cathode and anode. Finally, in order to work with feed voltages below 50 V, the electrical conductivity of the working fluid is increased by adding salt. A concentration of around  $2 \text{ g/dm}^3$  of salt was found adequate for the tap water used in our tests.

*2.3. Thermal-hydraulic tests*

A schematic diagram of the experimental set-up is shown in Fig. 3. It consists of three independent circuits. The second and third circuits are used to regulate the temperature of the reservoir tank (1). Test fluid was pumped from the open reservoir tank (1) by a train of three variable-speed gear pumps (2), which worked individually or simultaneously during the tests. The flow rate was measured by a Coriolis flow-meter (3). The baffles are installed in the main circuit (5). The test section was a thin-walled, 2 m long, 316L stainless steel tube with 37 equally-spaced insert baffles. The inner and outer diameters of the tube were 32 mm and 35 mm, respectively.

Heat transfer experiments were carried out under uniform heat flux (UHF) conditions. The tube was heated by Joule effect through AC in the tube wall. Power was supplied by a 6 kVA transformer (9) connected with copper electrodes to the tube. A variable auto-transformer was used for power regulation. The loop was insulated by an elastomeric thermal insulation material to minimize heat losses. The overall electrical power added to the heating section was calculated by measuring the voltage between electrodes and the electrical current. Fluid inlet (4) and outlet (7) temperatures were measured by submerged type RTDs (Resistance Temperature Detector).

Fig. 1 shows the wall temperature measurement lay-out installed along the test section, using T-type thermocouples. The wall temperature measurement Section (6) starts at a distance  $19.5D$  downstream of the first electrode, which corresponds physically to 13 cell lengths (or spacings between consecutive baffles),  $L$ . This ensures that the flow is thermally developed (spatially-periodic). A total number of 64 thermocouples peripherally distributed along eight axial sections on the outside wall cover two consecutive mixing tanks, following the sketches of Fig. 1. This arrangement is aimed at detecting the circumferential temperature gradient due to the flow stratification in the laminar region, and the axial temperature variations due to the local flow characteristics that occur between consecutive baffles.

Pressure drop tests were carried out under isothermal conditions. In order to capture the characteristics of the spatially-periodic flow, the first pressure port is placed in the fifth

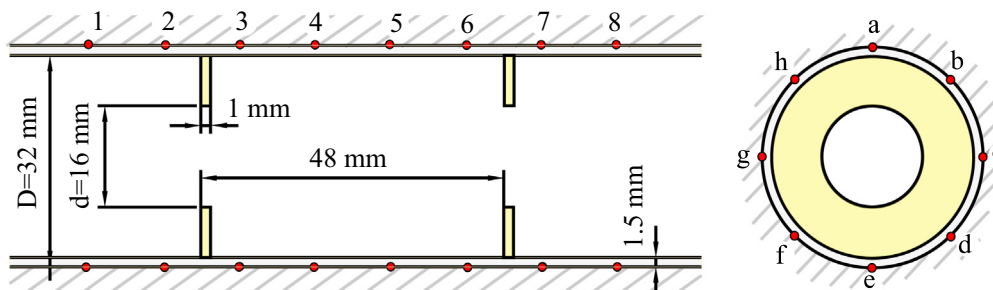


Fig. 1. Baffle geometry and thermocouple arrangement in the test section.

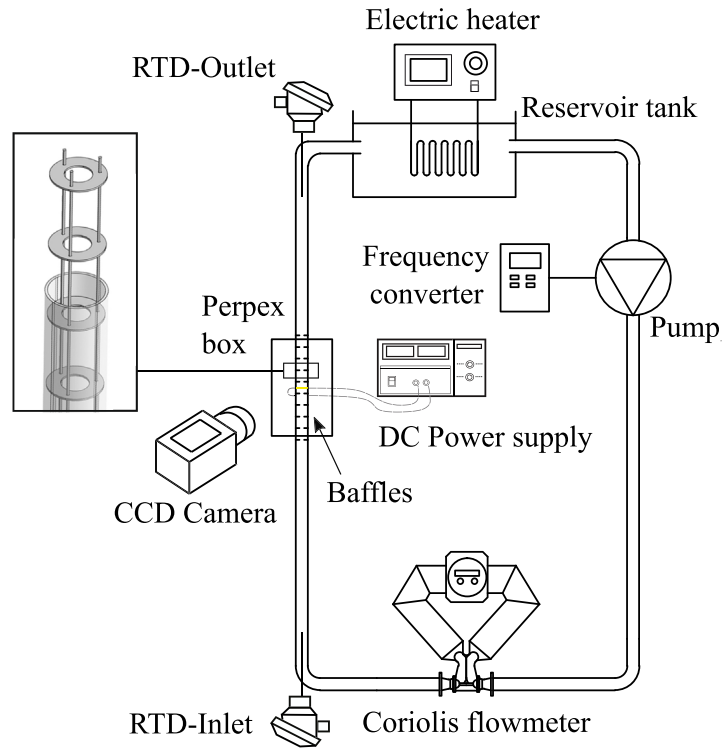


Fig. 2. Experimental setup for hydrogen bubble visualization.

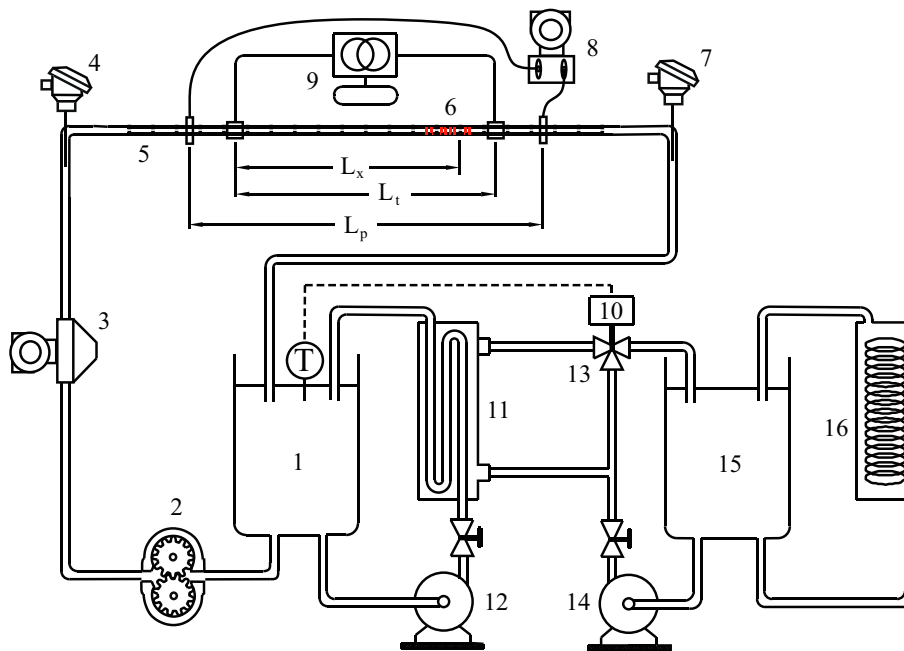


Fig. 3. Experimental set-up. (1) Reservoir tank, (2) Pumping system, (3) Coriolis Flowmeter, (4) PT-100 Class B 1/10 DIN temperature sensors, Inlet, (5) Baffles, (6) Wall thermocouples, (7) PT100, Outlet, (8) Pressure transducer, (9) Autotransformer, (10) PID Controller, (11) Heat Exchanger, (12) Centrifugal Pump, (13) Three way valve, (14) Centrifugal Pump, (15) Reservoir tank, (16) Chiller.

inter-baffle spacing. The second pressure port is located in the twenty-seventh inter-baffle spacing, which falls at a distance  $L_p = 1.296$  m downstream. Four pressure holes separated by  $90^\circ$  are made in the pressure connections in order to accommodate any peripheral disturbances of the static pressure. A set of highly accurate capacitive differential pressure transducers (8), with range: 0–10 mbar, 0–50 mbar, 5–500 mbar, 22–2500 mbar, were

employed to measure the pressure drop along the test section. Propylene-glycol is used as the working fluid. To ensure the right characterization of the fluid viscosity, a calibrated Cannon–Fenske viscometer is used periodically. Based on the viscosity measurement, an accurate (0.2% relative error) estimation of the propylene-glycol concentration can be derived from the tabulated data in [24]. Once the concentration is known, the other

thermophysical properties (density, specific heat and thermal conductivity) have been obtained by interpolation from the same reference [24]. Thus, this methodology considers the water presence in the tested fluid due to the high hygroscopicity of the propylene-glycol. The estimated error in the propylene-glycol concentration has been considered to quantify the uncertainty in the fluid properties in the later global uncertainty analysis.

The fluid temperature in the main tank is regulated by two additional circuits, with a variation of 0.1 °C of the target temperature. The third circuit consists of a thermal damping tank (15) filled with a water-glycerol mixture, whose temperature is adjusted using a chiller (16). From this tank, the chilled water is pumped (14) to a heat exchanger (11), to absorb the extra-heat from the test fluid, which is pumped to the heat exchanger using a centrifugal pump (12). A PID controller (10) adjusts the three-way valve (13) for controlling the flow rate of chilled water through the heat exchanger and, consequently, the heat transfer rate.

#### 2.4. Data reduction

Two different calibration tests were performed in order to conduct the heat transfer experiments appropriately. Firstly, calibration of the wall thermocouples was achieved by circulating very high flow rates of fluid at different temperatures. Steady-state measurements of the inlet and outlet temperatures and evaluation of the conduction thermal resistances across tube wall and insulation, allowed us to calibrate them, taking into account any contact resistance with the tube wall. Secondly, heat losses to the ambient were evaluated by measuring the fluid inlet and outlet temperatures when low flow rates were circulated through the test section at different temperatures.

The circumferential average Nusselt number is calculated at each section,  $j$ , using the following expression:

$$\bar{Nu}_j = \frac{q''}{T_{w_{ij}} - T_{b_j}} \cdot \frac{D}{k} \quad (1)$$

where  $q''$  is the generated heat (the voltage times the electric current) minus the heat losses along the test section, per heated area.  $T_{w_{ij}}$  is the averaged inner wall temperature at the  $j$  section, which is calculated using a two-dimensional numerical model which solves the radial and axial heat conduction equation in the tube wall.  $T_{b_j}$  is the bulk fluid temperature at the section  $j$ . Since the heat was added uniformly along the tube length,  $T_{b_j}$  was calculated by considering a linear variation with the axial direction, according to:

$$T_{b_j} = T_{b_{in}} + \frac{q}{\dot{m}c_p} \cdot \frac{x_j}{L_h} \quad (2)$$

where  $T_{b_i}$  is the fluid temperature at the inlet of the test section and  $x_j$  is the axial distance between the test section  $j$  and the point where the tube heating starts. The circumferential average Nusselt number is corrected by the factor  $(\mu_{w_i}/\mu_{w_b})^{0.14}$  to account for the change in the physical properties due to the radial temperature gradient [25]. Finally, the axial-averaged Nusselt number is calculated as:

$$\bar{Nu} = \frac{\sum_{j=1}^8 \bar{Nu}_j}{8} \quad (3)$$

Fanning friction factor was determined from the fluid mass flow rate and the pressure drop measurements as:

$$f = \frac{\rho \pi^2 D^5 \Delta p}{32 \dot{m}^2 L_p} \quad (4)$$

#### 2.5. Uncertainty analysis

The experimental uncertainty was calculated by following the ‘Guide to the expression of uncertainty in measurement’ published by ISO [26]. Instrumentation errors are summarized in Table 2. Uncertainty calculations based on a 95% confidence level showed limit values of 5.4% for Reynolds number, 3.9% for Prandtl number, 6.3% for Fanning friction factor and 2.3% for Nusselt number.

### 3. Numerical model

A 3D model of a tube with eight equally-spaced baffles is created and meshed using structured, hexahedral grid. A double compression ratio was introduced in both sides of the baffles, where greater variations of the flow pattern were expected due to the geometry constriction, and in radial direction, to ensure better solution where higher-velocity gradients were expected. The finite volume software ANSYS Fluent 18 was employed for the solution of the continuity and momentum pressure-based equations. Full Navier–Stokes equations were treated in general, body fitted coordinates. A control-volume storage scheme was employed where all variables were stored at the cell center. A second order upwind scheme was used in order to interpolate the face values of computed variables. An implicit segregated solver was used to solve the governing equations sequentially. In this study the pressure-velocity coupling algorithm SIMPLE was used. Steady-state simulations were solved in a first attempt, followed by the solution of the unsteady problem over a total time  $t = 10$  s, using a time step  $\Delta t = 0.1$  s, with a second-order discretization. This ensured a better convergence of the problem.

#### 3.1. Mesh independence study

A mesh independence study was accomplished to select the suitable size of the mesh. A total number of 5 meshes were simulated for the case with  $Re = 105$ , which is the highest Reynolds number that is simulated in this paper. In order to quantify the mesh independence, the axial velocity and the static pressure at the center of the cell are measured for each mesh. The deviation of these values from those obtained for the finest mesh provide a measurement of the independence of the mesh. The results, and the number elements for each mesh, are shown in Table 1.

As can be observed, the deviation of the mesh number 4 is less than one percent and can be considered as accurate enough. This mesh is used throughout the paper.

#### 3.2. Model validation

In order to validate the numerical model, we compared the pressure drop results from the numerical model and the experimental results, which are provided in Section 6.1. The mean deviation was around 7%. This deviation can be considered as satisfactory for the given purpose of the numerical model in this

**Table 1**  
Mesh independence study.

Mesh number	Elements · 10 <sup>3</sup> (per cell)	Static pressure, deviation (%)	Axial velocity, deviation (%)
1	85	12.5	11.8
2	140	6.2	5.6
3	188	3.1	1.2
<b>4</b>	<b>250</b>	<b>0.42</b>	<b>0.41</b>
5	410	–	–

**Table 2**  
Measurement uncertainties.

Measurement	Uncertainty
Bulk temperature	0.15 °C
Wall temperature	1.12 °C
Voltage	0.04% measure + 0.03% full scale
Intensity	0.1% measure + 0.04% full scale
Viscosity	3% measure
Pressure drop	0.2% measure
Thermal conductivity	0.9% measure
Specific heat	0.3% measure
Tube diameter	0.1% measure
Heat transfer section	0.01 m
Thermocouples position	0.005 m
Pressure test section	0.005 m

paper, which is to give a general perspective of the flow dynamics in the laminar region.

#### 4. Flow visualization results

Experiments were carried out for Reynolds numbers between 25 and 410. The results are shown at Fig. 4 and Fig. 5 in front and lateral views.

In Fig. 4(a), the front view for  $Re = 25$ , a core jet can be observed downstream the baffle, which gets broader along the cell and then narrower again upstream the next baffle. Besides, low velocities are detected in the peripheral region. For  $Re = 120$  the core jet has a uniform diameter along the interbaffle space, which is equal to the baffles orifice diameter,  $d$ . In Fig. 4(b), the bubbles generation was adjusted to show the recirculation of the outer region of the flow, which, again, has much lower velocities than the jet. By comparing the results for  $Re = 25$  and  $Re = 120$ , the recirculation in the outer region of the flow is observed to grow with the Reynolds number. The results for this range of Reynolds numbers ( $Re < 120$ ) show laminar flow conditions. This can be clearly

detected from the lateral view of the flow depicted in Fig. 5(a), where the hydrogen bubbles remain in the same plane.

At Reynolds number  $Re = 160$  (Fig. 4(c)), a similar core jet dominates the flow, although significant pulsations are detected. Such pulsations are also observed, in a higher frequency, in the lateral view for  $Re = 240$  in Fig. 5(b), where they result in part of the bubbles coming out of the symmetry plane.

For higher Reynolds numbers the flow becomes chaotic. The front view of the flow field for  $Re = 300$ , depicted in Fig. 4(d), shows no appreciable pattern but a disordered flow, while the lateral view provides qualitative information about a high mass transfer taking place in radial direction. The same flow behaviour is observed in the experiment at  $Re = 410$  in Fig. 5(c).

**Text for electronic version only:** The corresponding videos to the previous images can be also visualized. They show the front view of the flow seeded with hydrogen bubbles for:  $Re = 25$  (Video 1),  $Re = 120$  (Video 2),  $Re = 160$  (Video 3) and  $Re = 300$  (Video 4), and the lateral view for  $Re = 45$  (Video 5),  $Re = 240$  (Video 6) and  $Re = 410$  (Video 7).

#### 5. Numerical results

As could be observed in the previous section, the flow pattern seems to play a key role at low Reynolds numbers before the onset of the transition. The flow pattern is studied in more detailed in this subsection. Several simulations have been performed in the laminar flow regime, from  $Re = 1$  to  $Re = 150$ . The results, showing the velocity magnitude and the streamlines for a meridional plane along a cell (space between baffles), are represented in Fig. 6 for four Reynolds numbers.

For the lowest Reynolds number simulated (Fig. 6(a)),  $Re = 1$ , the core stream expands, after flowing through the baffle, and grows up to the walls. Despite the low Reynolds number, a tiny recirculation can be already seen downstream the baffles. For  $Re = 15$ , Fig. 6(b), the core stream still reaches the wall after

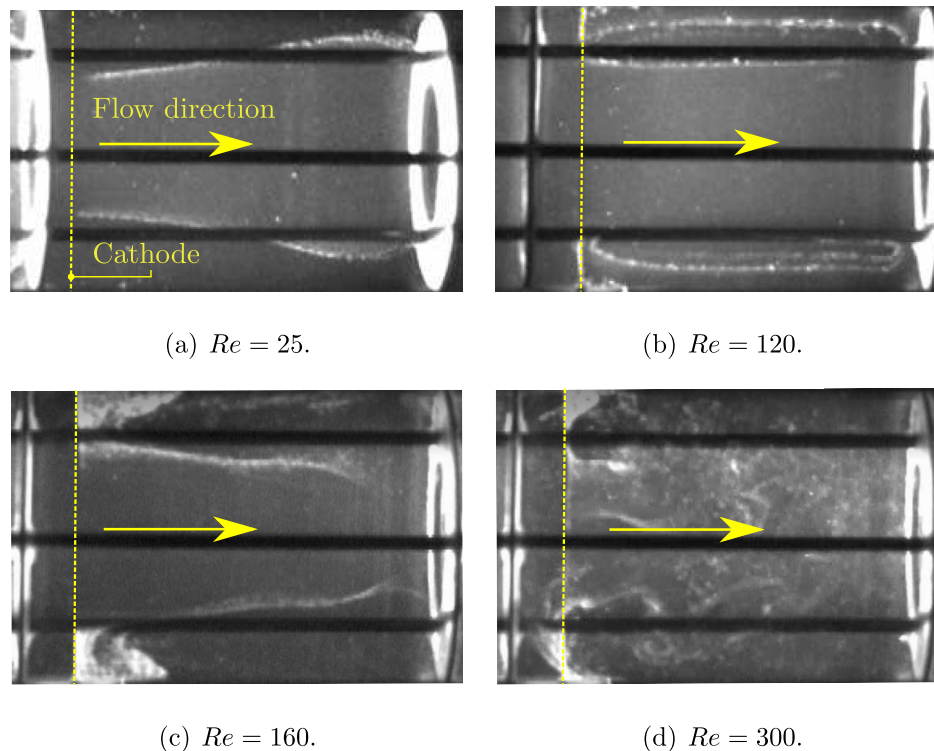
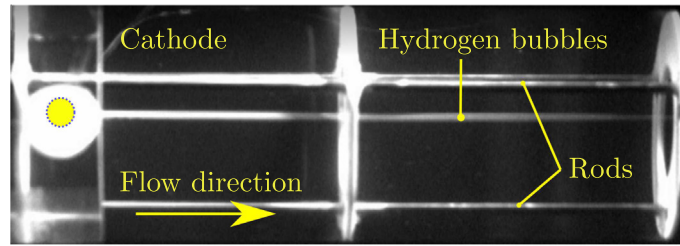
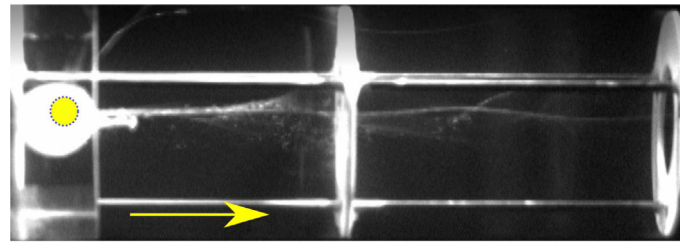


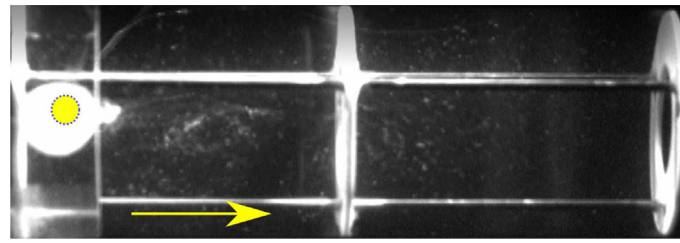
**Fig. 4.** Front view of the flow seeded with hydrogen bubbles for different Reynolds numbers.



(a)  $Re = 45$ .

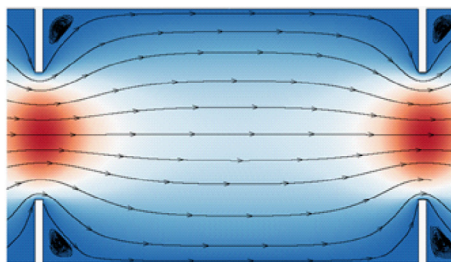


(b)  $Re = 240$ .

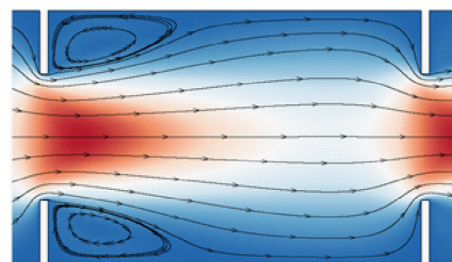


(c)  $Re = 410$ .

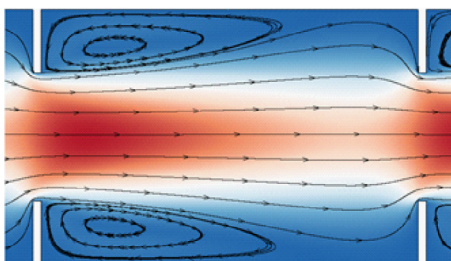
**Fig. 5.** Lateral view of the flow seeded with hydrogen bubbles for different Reynolds numbers.



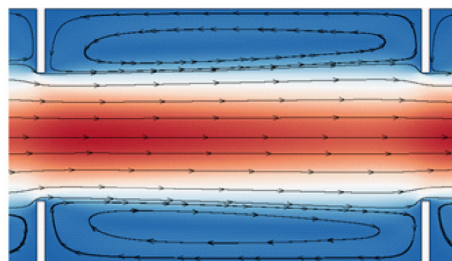
(a)  $Re = 1$ .



(b)  $Re = 15$ .



(c)  $Re = 32$ .



(d)  $Re = 105$ .

**Fig. 6.** CFD contour of non-dimensional velocity,  $v/v_{med}$  in the symmetry plane of the OBR.

expanding, but the recirculation has grown substantially. A limit case can be seen at  $Re = 32$ , Fig. 6(c), the core stream is not able to fully expand before reaching the next baffle. The recirculation fills more than one half of the interbaffle spacing. The extreme case corresponds to the pattern at  $Re = 102$ , Fig. 6(d), the core stream expands very slightly, and the recirculation fills all the space between consecutive baffles, this way, the flow can be described as a short-circuit between baffles.

In order to quantify the evolution of the size of the recirculation area, the recirculation size is calculated by measuring the average distance from the baffle for which the axial velocity reverses. A non-dimensional definition of this size for different Reynolds numbers is presented in Fig. 7. The graph shows a growth of the recirculation bubble with the Reynolds number, which ranges from a tiny size ( $l_{rec}/D = 0.04$ ) at  $Re = 1$  to the maximum achievable value, which is the interbaffle spacing,  $L$ , at  $Re = 70$ .

## 6. Thermal-hydraulic results

### 6.1. Pressure drop

In this subsection, the main pressure drop results are presented for Reynolds numbers from  $Re = 7$  to  $Re = 3000$ , and the different flow regions are identified [27].

Fig. 8(a) shows experimental results of the Fanning friction factor versus the Reynolds number. The analytical solution for a smooth tube in the laminar flow regime and the result obtained for an orifice plate, with an orifice coefficient equals to 0.8, are represented as well. Following the methodology proposed by Meyer and Olivier [28], the standard deviation of the pressure drop signal, sampled at a frequency of 2 Hz, divided by the mean pressure drop is also presented in Fig. 8(b).

The delimitation of the different flow regimes was performed according to the methodology proposed by Everts and Meyer [27]. Thus, the first and second derivatives of the Fanning friction factor with respect to Reynolds number are plotted in Fig. 9 for a fluid temperature of 60 °C.

The start of the transitional region was determined as the Reynolds number for which the first derivative of the Fanning friction factor was zero (point 'a' in Fig. 9(a)). This value can be visualized as the minimum in the Fanning friction factor at the end of the laminar flow regime. The start of the quasi-turbulent flow regime (point 'c' in Fig. 9(b)) was measured indirectly, calculating the point where the second derivative was zero (point 'b' in Fig. 9(b)), which corresponds to the middle point of the transitional

region [27]. Finally, the start of the turbulent flow regime could not be obtained from the derivative of well-known correlations for the turbulent flow region as the authors did. However, a linear method based on the method described by Meyer and Abolarin [29] was implemented. The proposed method consists in detecting the Reynolds number which divides the quasi-turbulent and turbulent regions and ensures the best fitting of a linear (in logarithmic axes) correlation for each region. The best fitting corresponds to the lowest mean deviation between the two correlations and the experimental data of their corresponding regions, quasi-turbulent and turbulent. The intersection of both linear correlations (point 'd' in Fig. 9(b)) marks the start of the turbulent region.

A brief discussion of the main characteristics observed in each flow regime is now given:

**Region I**, laminar flow regime:  $Re < 165$

In this region, the flow presents characteristics of laminar flow, with a strong influence of the Reynolds number on the friction factor, which agrees with the visualization results showed in Section 4. Likewise, the low fluctuation of the pressure drop signal -which is the lowest among all the regions- is a good measure of the steadiness of the flow. Friction factor augmentations of about 8 times, compared to the smooth tube, are identified. Pressure drop in this region can be estimated by the following correlation, which matches the experimental results with an accuracy of 10%:

$$f = 36.5Re^{-0.709} \quad 7 < Re < 165 \quad (5)$$

**Region II**, transitional flow regime:  $165 < Re < 235$

An abrupt change in friction factor in this region indicates the onset of transition to turbulence. Intense fluctuations of the pressure drop signal are identified in Fig. 8(b) in this region, which correspond to the unstable behavior that has also been detected in the flow visualization tests for the same operational regime (see Figs. 4(c) and 5(b), and the corresponding videos). These high fluctuations have also been observed in smooth tubes and tubes with helical fins during the transitional flow regime [28].

**Region III**, quasi-turbulent flow regime:  $235 < Re < 490$

The quasi-turbulent flow regime is characterized by a significant reduction in the slope of the Fanning friction factor (Fig. 8(a)). At the same time, the fluctuations of the pressure drop measurements are reduced (Fig. 8(b)). Nevertheless, this region should be distinguished because the turbulence is not fully developed and a correlation obtained for the turbulent region would over-predict the friction factor. A correlation is obtained:

$$f = 0.753Re^{0.209} \quad 235 < Re < 490 \quad (6)$$

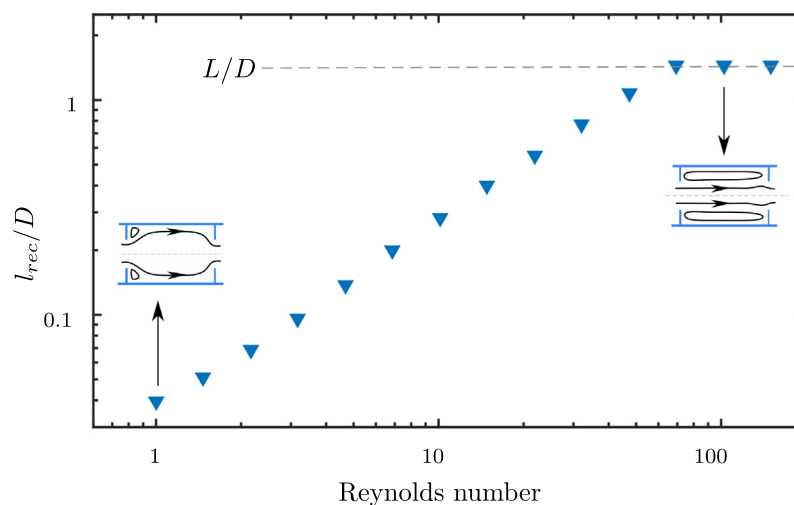
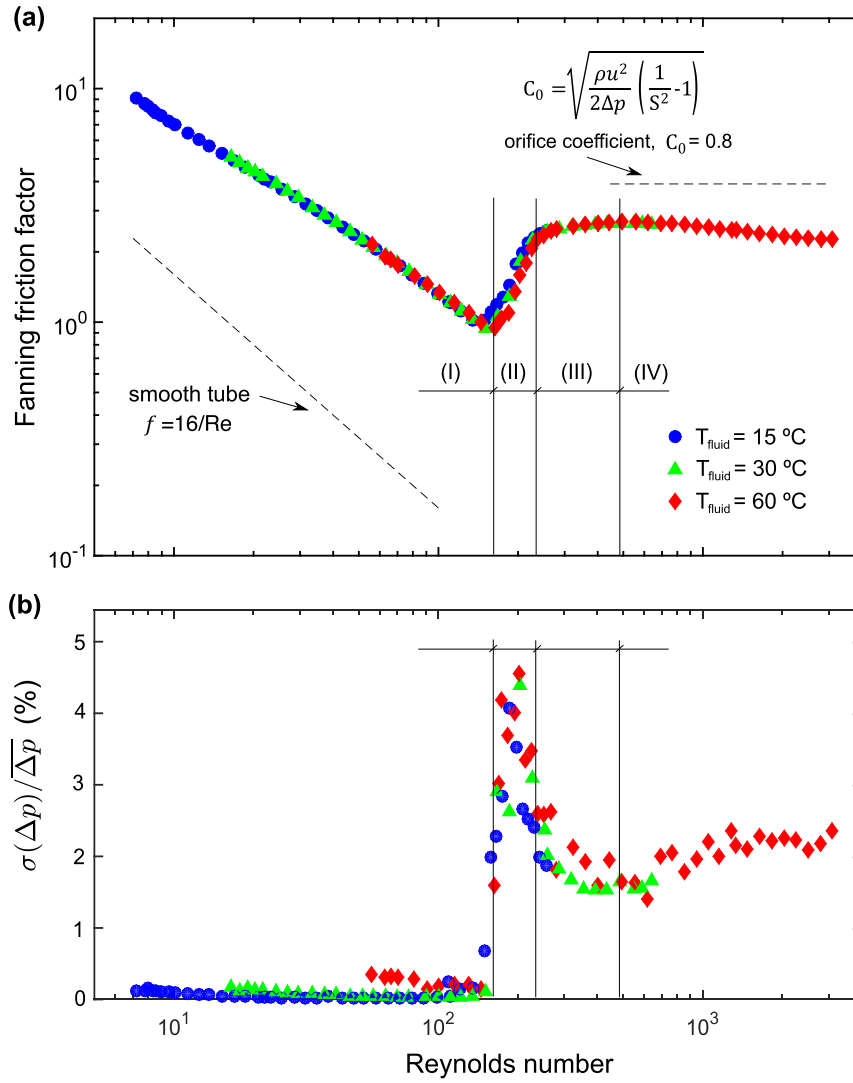
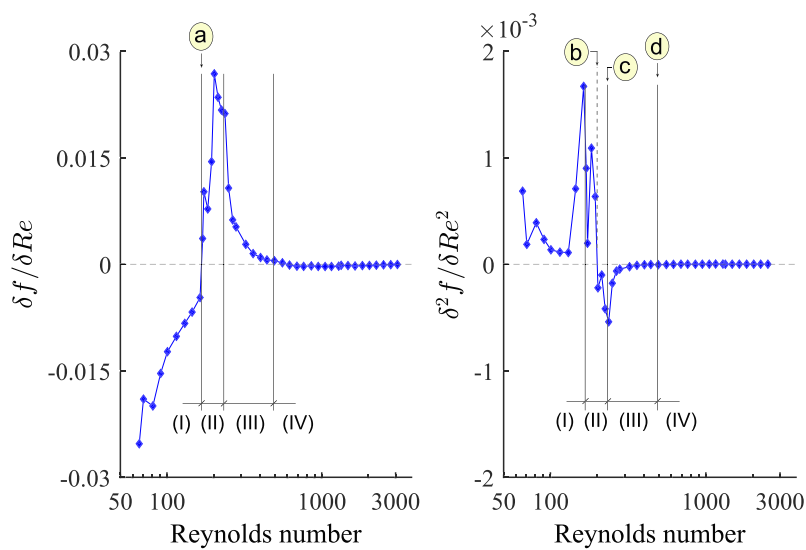


Fig. 7. Recirculation zone size as a function of the Reynolds number.



**Fig. 8.** (a) Fanning friction factor vs Reynolds number for several tested fluid temperatures. (b) Standard deviation of the pressure measurements vs Reynolds number for several tested fluid temperatures.



**Fig. 9.** (a) First and (b) second derivatives of the Fanning friction factor with respect to Reynolds number as a function of the Reynolds number. Fluid temperature equals to  $60^\circ C$ .

**Region IV, turbulent flow regime:**  $Re > 490$

The turbulent flow regime is achieved from  $Re \approx 490$  onwards. The standard deviation of the pressure signal is stabilized, with higher values than those of the laminar flow regime and similar to the quasi-turbulent flow regime. This reduction in the pressure drop fluctuations was also observed by Meyer and Olivier [28], but in their case the fluctuations beyond the transitional region were similar to the values obtained in the laminar flow region. In our case, the fluctuations in the quasi-turbulent and turbulent regions are much higher than in the laminar region, around 5 times. The discrepancy can be justified by the significant differences in the tested geometries, i.e., smooth or finned tubes vs tubes with transverse baffles.

The relatively low influence of the Reynolds number on the friction factor is also noticeable. The following correlation is proposed for the range  $490 < Re < 3000$ , which meets all the experimental results with an accuracy of 8%:

$$f = 5.34Re^{-0.107} \quad 490 < Re < 3000 \quad (7)$$

As reflected in Fig. 8(a), the friction factor is much lower than the one expected for an orifice with the same open area ratio. This can be justified by the interaction between consecutive baffles, after crossing a baffle the flow is not developed before reaching the next one, so the effect can not be described as a series of independent baffles.

**6.2. Heat transfer**

In this subsection, the main heat transfer results are provided for Reynolds numbers from 10 to 2200, and Prandtl numbers from 150 to 630. Fig. 10 shows experimental results of the Nusselt number as a function of the Reynolds number for three Prandtl numbers,  $Pr = 150, 285$  and  $630$ . For the sake of comparison, the corresponding Nusselt number for a smooth tube under developed mixed convection is presented [30].

Based on the influence of the Reynolds number, three different flow regions can be clearly distinguished: laminar (I), transitional (II) and turbulent (IV). It should be noticed that the quasi-turbulent (III) region has not be distinguished from the transitional region. A detailed analysis to delimit all the flow regions could not be performed, due to the lower resolution of the acquired data. In order to preserve the coherence throughout the paper, the nomenclature for the four regions is maintained in the following figures. But, the term transitional region is assumed to include the quasi-turbulent region from now on.

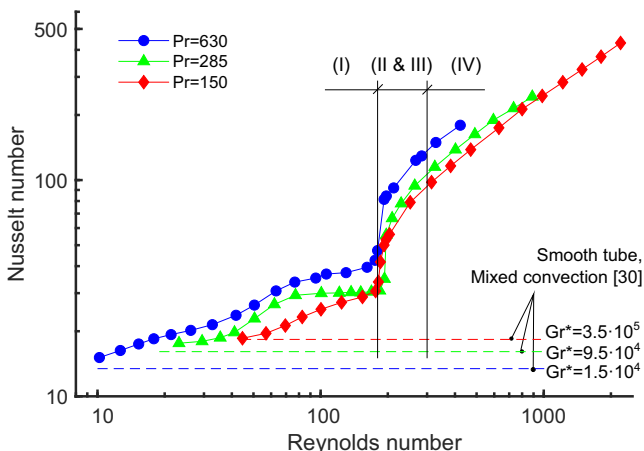


**Fig. 10.** Nusselt number vs Reynolds number for three Prandtl numbers.

In the laminar region,  $Re < 160$ , there is a low influence of the Reynolds number on heat transfer coefficients, which are significantly higher than those which would be obtained for a smooth tube working under mixed convection conditions, especially at the higher Prandtl numbers.

The Reynolds number influence is quite sharp in the transitional region,  $160 < Re < 300$ . Onwards, the onset of turbulence highly increases the heat transfer rates. This outbreak occurs for  $Re > 300$ , which proves the suitability of the insert baffles as turbulence promoters for heat transfer increment purposes.

These data can be adjusted to correlations which as well show the influence of the Reynolds and Prandtl numbers on the Nusselt number. Eq. (8) corresponds to region I (laminar) and Eq. (9) to region IV (turbulent).

$$Nu = 1.304Re^{0.402}Pr^{0.227} \quad 10 < Re < 100 \quad (8)$$

$$Nu = 0.503Re^{0.735}Pr^{0.216} \quad 300 < Re < 2200 \quad (9)$$

These equations are suitable for the Prandtl number range  $130 < Pr < 650$ . The exponent of the Prandtl number is similar for both regions (considering the experimental error). The fitting is quite satisfactory for both regions, with all the experimental results included in a range of  $\pm 10\%$  of the correlation, as can be seen in Fig. 11.

A different way to identify the end of the laminar flow regime is using the standard deviation of the wall temperature [29]. Fig. 12 shows the mean standard deviation of all the measured wall temperatures as a function of the Reynolds number. For low Reynolds numbers the standard deviation is low and corresponds to the measurement noise. A significant increase for  $Re > 160$  indicates the onset of the transitional regime, when the flow pulsation allows the colder central stream to contact the wall regions, increasing the wall temperature fluctuations. Above  $Re = 300$ , the value is higher than in the laminar region but stable again, pointing the onset of the turbulent regime.

**6.3. Performance evaluation**

In order to evaluate the thermal enhancement of the geometry tested, the R3 criterion is used [31]. This parameter measures the heat transfer ratio between the tested geometry and an equivalent smooth tube for the same power consumption and basic geometry (number of tubes and tube diameter and length) (Eq. (10)).

$$R3 = \frac{Nu}{Nu_s} \Big|_{\dot{W}=\dot{W}_s, N=N_s, D=D_s, l=l_s} \quad (10)$$

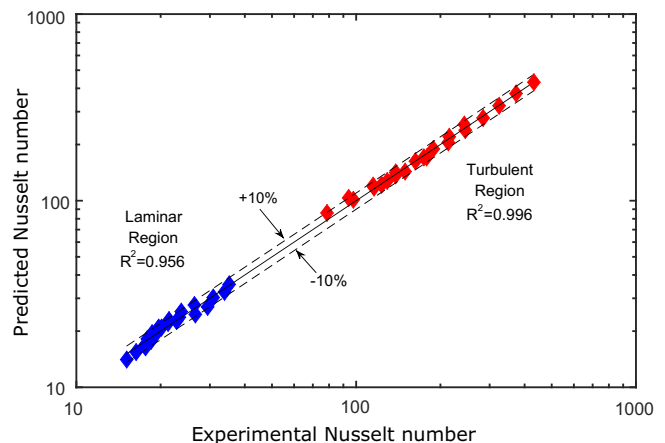


**Fig. 11.** Comparison of the experimental Nusselt number and the predicted Nusselt number using Eqs. (8) and (9).

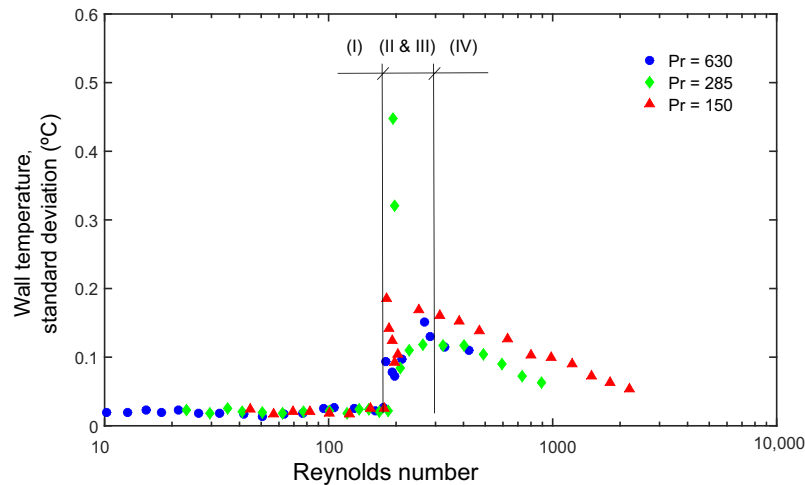


Fig. 12. Standard deviation of the wall temperature vs Reynolds number.

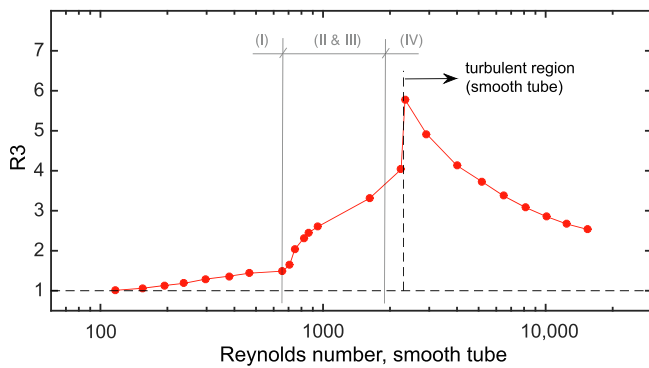


Fig. 13. Performance evaluation criteria R3 vs smooth tube Reynolds number,  $Pr = 150$ .

For the same power consumption, well-known correlations of Nusselt number for the laminar ([30],  $Re < 2300$ ), transitional ([32],  $2300 < Re < 4000$ ) and turbulent ([33],  $Re > 4000$ ) flow regimes are used for calculating the term  $Nu_s$ . The results for  $Pr = 150$  are represented in Fig. 13.

As can be observed, the circular-orifice baffles show a poor performance for  $Re_s < 700$ , and a slight increase in the thermal performance with the Reynolds number. This is due to the increase in the Nusselt number in the laminar region when the  $Re$  is increased. Above  $Re_s = 800$  there is a sharp rise in the thermal performance due to the onset of the transitional regime in the baffled tube. So, the range  $800 < Re_s < 2300$  is where the highest performance can be expected. This trend is cut by the onset of the transitional regime in the smooth tube at  $Re_s = 2300$ , generating a descending trend in the performance. However, there is enhancement for all the range tested in the turbulent flow regime, with the lowest performance,  $R3 \sim 2.5$ , at  $Re_s \approx 2 \times 10^4$ .

## Conclusions

- An extensive study has been done in order to quantify the thermo-hydraulic performance of tubes with periodically-spaced circular-orifice baffles. A wide range of dimensionless numbers has been studied ( $Pr = 150 - 630$ ,  $Re_n = 10 - 2200$ ).
- Qualitative flow visualization tests show the flow patterns in the baffled tube in the three different flow regimes. In the laminar region, the size of the recirculation zones under the baffles

characterizes the flow. Instability can be observed for  $Re > 160$ , this instability of the flow is related to the pulsation of the core stream. For  $Re > 300$  the flow can be described as chaotic.

- Pressure drop and heat transfer measurements demonstrate the existence of four flow regions with distinguishable characteristics: a laminar region ( $Re < 160$ ), a transitional and a quasi-turbulent region ( $160 < Re < 300$ ) and a turbulent region ( $Re > 300$ ).
- The R3 performance criteria shows that the tested geometry can be advantageous, for  $Pr = 150$ , in comparison to smooth tubes working at a Reynolds number between 100 and  $2 \cdot 10^4$ .

## Declaration of Competing Interest

There is no conflict of interest.

## Acknowledgements

The authors gratefully acknowledge the financial support of the project DPI2015-661943-P by Ministerio de Economía y Competitividad (MINECO, Spain) and the Fondo Europeo de Desarrollo Regional (FEDER). The authors are grateful to SEDIC-SAIT (UPCT) for providing the technical resources for CFD computations.

## Appendix A. Supplementary material

Supplementary data associated with this article can be found, in the online version, at <https://doi.org/10.1016/j.ijheatmasstransfer.2019.118914>.

## References

- [1] R. Manglik, A. Bergles, Heat transfer and pressure drop correlations for twisted tape inserts in isothermal tubes: Part I—Laminar flows, *J. Heat Transfer* 115 (4) (1993) 881–889.
- [2] R. Manglik, A. Bergles, Heat transfer and pressure drop correlations for twisted-tape inserts in isothermal tubes: Part II—transition and turbulent flows, *J. Heat Transfer* 115 (4) (1993) 890–896.
- [3] S.M. Abolarin, M. Everts, J.P. Meyer, Heat transfer and pressure drop characteristics of alternating clockwise and counter clockwise twisted tape inserts in the transitional flow regime, *Int. J. Heat Mass Transf.* 133 (2019) 203–217.
- [4] T. Ravigururajan, A. Bergles, Development and verification of general correlations for pressure drop and heat transfer in single-phase turbulent flow in enhanced tubes, *Exp. Thermal Fluid Sci.* 13 (1) (1996) 55–70.
- [5] A. Garcia, P.G. Vicente, A. Viedma, Experimental study of heat transfer enhancement with wire coil inserts in laminar-transition-turbulent regimes

- at different Prandtl numbers, *Int. J. Heat Mass Transf.* 48 (21–22) (2005) 4640–4651.
- [6] P. Drögemüller, The use of hiTRAN wire matrix elements to improve the thermal efficiency of tubular heat exchangers in single and two-phase flow, *Chem. Ing. Tech.* 87 (3) (2015) 188–202.
- [7] V. Kongkaiatpaiboon, K. Nanan, S. Eiamsa-ard, Experimental investigation of convective heat transfer and pressure loss in a round tube fitted with circular-ring turbulators, *Int. Commun. Heat Mass Transfer* 37 (5) (2010) 568–574.
- [8] P. Promvong, N. Koolnapadol, M. Pimsarn, C. Thianpong, Thermal performance enhancement in a heat exchanger tube fitted with inclined vortex rings, *Appl. Therm. Eng.* 62 (1) (2014) 285–292.
- [9] A. Acir, I. Ata, M.E. Canli, Investigation of effect of the circular ring turbulators on heat transfer augmentation and fluid flow characteristic of solar air heater, *Exp. Thermal Fluid Sci.* 77 (2016) 45–54.
- [10] K. Ruengpayungsak, K. Wongcharee, C. Thianpong, M. Pimsarn, V. Chuwattanakul, S. Eiamsa-ard, Heat transfer evaluation of turbulent flows through gear-ring elements, *Appl. Therm. Eng.* 123 (2017) 991–1005.
- [11] S. Eiamsa-Ard, V. Kongkaiatpaiboon, K. Nanan, Thermohydraulics of turbulent flow through heat exchanger tubes fitted with circular-rings and twisted tapes, *Chin. J. Chem. Eng.* 21 (6) (2013) 585–593.
- [12] S.M. Abolarin, M. Everts, J.P. Meyer, The influence of peripheral u-cut twisted tapes and ring inserts on the heat transfer and pressure drop characteristics in the transitional flow regime, *Int. J. Heat Mass Transf.* 132 (2019) 970–984.
- [13] X. Ni, M. Mackley, A. Harvey, P. Stonestreet, M. Baird, N. Rama Rao, Mixing through oscillations and pulsations—A guide to achieving process enhancements in the chemical and process industries, *Chem. Eng. Res. Des.* 81 (3) (2003) 373–383.
- [14] M.R. Mackley, P. Stonestreet, Heat transfer and associated energy dissipation for oscillatory flow in baffled tubes, *Chem. Eng.* 50 (14) (1995) 2211–2224.
- [15] Paste Particle and Polymer Processing group (P4G), Oscillatory Fluid Mixing, OFM: Enhancement of heat transfer rates.
- [16] R. Law, S. Ahmed, N. Tang, A. Phan, A. Harvey, Development of a more robust correlation for predicting heat transfer performance in oscillatory baffled reactors, *Chem. Eng. Process. - Process Intensif.* 125 (December 2017) (2018) 133–138.
- [17] D. González-Juárez, R. Herrero-Martín, J.P. Solano, Enhanced heat transfer and power dissipation in oscillatory-flow tubes with circular-orifice baffles: a numerical study, *Appl. Therm. Eng.* 141 (January) (2018) 494–502.
- [18] R. Kiml, A. Magda, S. Mochizuki, A. Murata, Rib-induced secondary flow effects on local circumferential heat transfer distribution inside a circular rib-roughened tube, *Int. J. Heat Mass Transf.* 47 (6–7) (2004) 1403–1412.
- [19] J. Muñoz, D. Crespi, J.P. Solano, P.G. Vicente, On the early onset of transition in circular-orifice baffled tubes: an experimental study, in: *Proceedings of the Ninth International Symposium on Turbulence, Heat and Mass Transfer*, 2018, pp. 561–564.
- [20] A.C. Jealous, H.F. Johnson, Power requirements for pulse generation in pulse columns, *Ind. Eng. Chem.* 47 (6) (2005) 1159–1166.
- [21] F. Johansen, Flow through pipe orifices at low Reynolds numbers, *Proc. Roy. Soc. London* 126 (801) (1930) 231–245.
- [22] X. Ni, G. Brogan, A. Struthers, D.C. Bennett, S.F. Wilson, A systematic study of the effect of geometrical parameters on mixing time in oscillatory baffled columns, *Chem. Eng. Res. Des.* 76 (A5) (1998) 635–642.
- [23] F.A. Schraub, S.J. Kline, J. Henry, P.W. Runstadler, A. Littell, Use of hydrogen bubbles for quantitative determination of time-dependent velocity fields in low-speed water flows, *J. Basic Eng.* 8 (2) (1965) 429–444.
- [24] A.H. ASHRAE, *Fundamentals 2001*, American Society of Heating, Refrigerating, and Air-Conditioning Engineers, Atlanta, GA, 2001.
- [25] E.N. Sieder, G.E. Tate, Heat transfer and pressure drop of liquids in tubes, *Ind. Eng. Chem.* 28 (12) (1936) 1429–1435.
- [26] ISO, *Guide to the Expression of Uncertainty in Measurement*, 1st ed., International Organization for Standardization, Switzerland, 1995.
- [27] M. Everts, J.P. Meyer, Heat transfer of developing and fully developed flow in smooth horizontal tubes in the transitional flow regime, *Int. J. Heat Mass Transf.* 117 (2018) 1331–1351.
- [28] J.P. Meyer, J.A. Olivier, Transitional flow inside enhanced tubes for fully developed and developing flow with different types of inlet disturbances: Part I - Adiabatic pressure drops, *Int. J. Heat Mass Transf.* 54 (2011) 1587–1597.
- [29] J.P. Meyer, S.M. Abolarin, Heat transfer and pressure drop in the transitional flow regime for a smooth circular tube with twisted tape inserts and a square-edged inlet, *Int. J. Heat Mass Transf.* 117 (2018) 11–29.
- [30] B.S. Petukhov, A.F. Polyakov, *Heat Transfer in Laminar Mixed Convection*, 1st ed., Hemisphere, New York, 1988, pp. 57–89 (Ch. 3).
- [31] A. Bergles, A. Blumenkrantz, J. Taborek, Performance evaluation criteria for enhanced heat transfer surfaces, in: *Proceedings of the 5th International Heat Transfer Conference*, vol. 2, Tokyo, Japan, 1974, pp. 239–243.
- [32] V. Gnielinski, On heat transfer in tubes, *Int. J. Heat Mass Transf.* 63 (2013) 134–140.
- [33] V. Gnielinski, New equations for heat and mass transfer in turbulent pipe and channel flow, *Int. Chem. Eng.* 16 (2) (1976) 359–368.